Inert Gas Enhanced Laser-Assisted Purification of Platinum Electron-Beam-Induced Deposits

Michael G. Stanford[1], Brett B. Lewis[1], Joo Hyon Noh[1], Jason D. Fowlkes[1,2], and Philip D. Rack[1,2*]

1) Materials Science and Engineering Department, University of Tennessee, Knoxville, TN 37996, USA
2) Nanofabrication Research Laboratory, Center for Nanophase Materials Sciences, Oak Ridge National Laboratory, Oak Ridge, TN 37381, USA

Keywords: Electron beam induced deposition, purification, atomic layer deposition, direct write, platinum

Abstract

Electron beam-induced deposition patterns, with composition of PtC_5, were purified using a pulsed laser induced purification reaction to erode the amorphous carbon matrix and form pure platinum deposits. Enhanced mobility of residual H_2O molecules via a localized injection of inert Ar-H_2 (4%) is attributed to be the reactive gas species for purification of the deposits. Surface purification of deposits was realized at laser exposure times as low as 0.1 s. The ex-situ purification reaction in the deposit interior was shown to be rate-limited by reactive gas diffusion into the deposit, and deposit contraction associated with the purification process caused some loss of shape retention. To circumvent the intrinsic flaws of the ex-situ anneal process, in-situ deposition and purification techniques were explored which resemble a direct write atomic layer deposition (ALD) process. First, we explored a laser assisted electron beam induced deposition (LAEBID) process augmented with reactive gas which resulted in a 75% carbon reduction compared to standard EBID. A sequential deposition plus purification process was also developed and resulted in deposition of pure platinum deposits with high fidelity and shape retention.

Introduction

Focused electron-beam-induced processing (FEBIP) is capable of directly depositing and etching material with nanoscale resolution[1–3]. Electron-beam-induced deposition (EBID) occurs when a precursor species is decomposed by a focused electron beam, resulting in a condensed deposit and some volatile reaction byproducts. This technique enables 3-dimensional direct write of nanoscale structures via an intelligent control of the focused electron beam raster sequence. An improved understanding of the fundamental electron-precursor-solid interactions have led to advances in growth rate and resolution of the EBID process[4–7]. These advancements have enabled the emergence of many applications for materials grown via the EBID technique such as direct write plasmonic structures[8,9], field-emission emitters[10,11], maskless lithography[12–15], lithography mask editing[16–18,19], scanning probe tips[20,21], superconducting nanostructures[22,23], electrical contacts[24], and nanomagnetic logic[25,26] to list a few.

Although EBID has been used for the aforementioned applications, a major liability has been the inclusion of unwanted byproducts in the final deposit. Since EBID is typically carried out at room temperature using standard chemical vapor deposition precursors, the precursor ligands do not completely volatilize via electron stimulated reactions. This results in the inclusion of unwanted ligands and ligand fragments in the deposit[27]. In the case of the commonly used organometallic trimethyl(methylcyclopentadienyl)-platinum(IV) ($MeCpPt^{IV}Me_3$), incomplete volatilization during the EBID process results in the inclusion of methyl ligands and other carbon rich byproducts. Hence the final deposit is a PtC_x material with $5 \leq x \leq 8$[28,29], that consist of platinum nanoparticles embedded within a hydrogenated amorphous carbon matrix. Many purification techniques have been explored to address the EBID contamination issue with varying success[1]. Some of these approaches include post and in-situ electron irradiation[30–33,34,35], use of more easily volatilized precursors[36–38], post deposition annealing[39–41], reactive gas co-flow[42–44], and in-situ substrate heating[39,45] to name a few. Martin et al. have recently demonstrated that inert gas flow can enhance electron-beam-induced etch rates of carbon, by increasing the flow of residual chamber reactive gases[46].

Recently, we have demonstrated enhanced purification of EBID deposits using an in-situ laser anneal technique. In this process, so-called laser assisted electron beam induced deposition (LAEBID), synchronized laser pulses were used to intermittently assist in the thermal desorption of byproducts after each electron beam pass[47]. This method was successful in improving deposit purity as well as spatial resolution of the direct write EBID process, however LAEBID could not completely purify the deposits. To promote further purification of EBID patterns deposited from the $MeCpPtMe_3$ organometallic precursor, we recently demonstrated an in-chamber pulsed laser-induced oxidation purification process[48]. The process was able to fully purify deposits in a minimally invasive manner via a photothermal oxidation reaction. Adversely, a 70% volumetric reduction upon removal of carbonaceous byproducts resulted in a loss in precise shape retention and fidelity of deposits.

To increase purity, shape retention, and fidelity of EBID deposits, here we have developed a laser-induced purification reaction using residual H_2O molecules as a reactive gas species whose mobility to the EBID reaction zone is enhanced by a localized flow of Ar or Ar-H_2 (4%). Furthermore, we explored in-situ strategies to deposit pure patterns which have cyclic deposition and purification steps. Specifically, we use an infrared pulsed laser delivery system mounted on a high angle port of a dual beam system to irradiate EBID deposits under a localized ambient of inert Ar-H_2 (4%) or Ar gas. While initially we attributed the purification process to be due to a localized hydrogenation from the localized 4% H_2, subsequent experiments demonstrated that a pure Ar flow also results in purification. Thus, as described below, the enhanced reaction is attributed to enhanced surface diffusion of residual H_2O molecules to the EBID deposit via the localized Ar gas injection. The deposits are photothermally heated and facilitate the dissociation of the H_2O molecules into O^*, H^*, and OH^* radicals and the radicals subsequently react with the carbonaceous matrix in the PtC_x to form volatile byproducts. Hence, hydrogenation and oxidation reactions are attributed with the removal of the carbonaceous matrix. We also demonstrate an in-situ reactive gas-assisted LAEBID process as well as a sequential deposition and purification technique. The later succeeds in depositing pure patterns with high shape retention and resembles a direct write ALD process with a first half-reaction driven by electron beam induced deposition and the second half-reaction driven by the photothermal hydrogenation reaction with the carbon byproducts. In this work, the terminology “ALD” is not used to reflect that an exact monolayer of material is deposited per cycle. Rather “ALD” is used in the sense described by Kanarik et al.[49] which states that the process benefits from separate self-limiting half reactions with atomic-scale fidelity. Schematics illustrating the purification techniques studied here are shown in Figure 1.

Experimental

Electron-beam-induced deposition

EBID was performed using an FEI Nova Nanolab 600 Dual Beam system on a Si substrate with a 200 nm thick thermally grown silicon oxide layer. The chamber was air plasma cleaned with an Evactron system, produced by XEI Scientific Inc., for a minimum of 15 minutes prior to deposition. Unless noted, EBID was carried out by locally injecting $MeCpPtMe_3$ precursor in close proximity to the area of interest where the GIS needle was positioned ~100 μm above the substrate and ~ 200 μm from the center of the field of view. The $MeCpPtMe_3$ crucible was heated to approximately 45°C to increase the vapor pressure of the precursor. The chamber pressure was ~ 1.0×10^{-5} mbar during injection of the $MeCpPtMe_3$ precursor into the chamber with a base pressure of ~ 1.0×10^{-6} mbar. Each pattern was deposited using 5 keV electron beam energy, 98 pA beam current, 10 μs dwell time, and a 13.6 nm pixel pitch. The number of EBID passes were varied (1000, 2000, 4000, and 8000) to create deposits that were approximately 25, 50, 90, and 240 nm thick.

Pulsed laser reactive gas anneal

A 915 nm wavelength 25 W multichip diode laser module with model number BMU25B-915-01, produced by Oclaro Inc., was used to anneal the deposits. This laser module was driven by an IXYS PCX-7410 pulsed diode laser driver. A laser delivery system, produced by Omniprobe, Inc. (an Oxford Company), was mounted on a high angle port in the SEM chamber at an angle of

52° relative to the substrate. This system enabled the simultaneous delivery of an approximately 100 μm diameter laser spot size with a Gaussian distribution to the EBID deposit in the SEM chamber. Inert Ar gas was delivered to the area of interest using an OmniGIS I gas injection system; the inert gas contained a small mixture of H_2 gas (4 volume %). Subsequent comparisons with pure Ar gas, reveal that the H_2 species have no observable contribution toward the purification process. The needle was positioned ~100 μm above the sample and ~200 μm from the center of field of view. The chamber base pressure before reactive gas flow was ~ 1.0×10^{-6} mbar. The valve pulsing rates in the OmniGIS I, which ultimately control the reactive gas flux, were set to achieve a chamber pressure of 1.2×10^{-5} mbar when the reactive gas was flowing, and the gas temperature was 25 °C. The needle configuration for deposition and the subsequent purification are illustrated in Figure 2. For this work, the optical power density of the laser was constant at ~165 kW/cm^2. Laser pulse width and duty cycle were varied with the laser driver. Additional information on the laser delivery system can be found in reference[50]. The EBID and subsequent pulsed laser reactive gas anneal processes are illustrated in Figure 1a.

Reactive laser assisted electron-beam-induced deposition

Reactive laser assisted electron beam induced deposition (LAEBID) was carried out by performing EBID to deposit PtC_x patterns while simultaneously irradiating the EBID deposit with the pulsed laser in a Ar inert gas co-flow, where the Ar once again increases flux of the reactive gas (H_2O) to the deposit region. EBID was conducted using 5 keV electron beam energy, 98 pA beam current, 10 μs dwell time, and a 13.6 nm pixel pitch. A schematic of this process is illustrated in Figure 1b. Some LAEBID deposits included an additional 13.6 ms refresh time after each EBID pass to lengthen reactive gas annealing time per pass. During the EBID pass, the laser was simultaneously pulsed with either 10 μs or 100 μs pulsewidths. The irradiation duty cycle was varied over the range of 0.1% - 6% (see supplemental information for more details and Figure S1 which shows a schematic illustrating a map of laser and EBID synchronization). For this work, the FEI GIS for the $MeCpPtMe_3$ precursor gas as well as the OmniGIS I for the inert gas were opened concurrently to establish the co – flow regime. The partial pressures of the Ar inert gas and $MeCpPtMe_3$ precursor introduced into the chamber were approximately 1.10×10^{-5} mbar and 9.0×10^{-6} mbar, respectively. During the co-flow experiments, the precursor gas nozzle was retracted ~8 cm vertically and ~5 cm horizontally while the reactive gas GIS needle was positioned 100 μm above the sample and 200 μm from the center of field of view (see Figure 2). By comparison, in the typical EBID experiment the precursor gas nozzle is located in the same close position. Ultimately, this needle configuration significantly decreases the flux of $MeCpPtMe_3$ precursor gas molecules relative to the reactive gas molecules to slow the EBID growth and enhance the purification of the deposits.

Sequential or layer-by-layer EBID plus laser reactive gas anneal

As will be demonstrated, the co – flow of gases used in the LAEBID process, prohibit complete volatilization of unwanted byproducts in the final deposit. To circumvent the issues of the co-flow of precursor gas and reactive gas in the LAEBID process, a sequential deposition and purification process was also developed. In this process, precursor gas and Ar inert gas were injected (separately) into the chamber under standard EBID and laser annealing parameters. A 30 keV beam energy and 150 pA beam current were used for deposition in this study to minimize peripheral PtC_5 deposition on the substrate[51,52]. For the layer-by-layer process, an optimum EBID thickness per cycle was determined to be 70 nm (see supplemental information S4). After the EBID cycle, the precursor gas was pumped from the chamber until a base pressure of $\sim 2.0 \times 10^{-6}$ mbar was achieved and Ar inert gas was injected into the chamber to enhance flow rate of residual H_2O to the deposit at a pressure of ~1.2 x 10^{-5} mbar. The pulsed laser system was then used to irradiate the sample with 10 μs pulses at 1% duty cycle for a total laser exposure time of 3.0 s and equivalent process time of 5 minutes. After each cycle, the deposit was irradiated with several 100 μs laser pulses to initiate the coalescence of any disconnected Pt grains in the deposit. This step was required to mitigate the evolution of porosity in the final morphology. For the sequential approach, the needles for the reactive gas and precursor gas were both positioned 100 μm above the sample and 200 μm from the center of field of view (as shown in Figure 2). The sequential EBID + laser anneal process was repeated in order to create a pure deposit of desired size and shape and a schematic of this process is shown in Figure 1c.

Energy Dispersive Spectroscopy (EDS) Analysis

EDS spectra were recorded while irradiating the substrate with a 5 keV energy electron beam at a beam current of 1.6 nA. Analysis to determine the normalized carbon content of each spectra were conducted by first subtracting a background spectra of the underlying SiO_2 substrate. The Pt and C EDS signatures, located at 2.048 keV and 0.277 keV respectively, were then fit with a Gaussian curve of the form shown in equation 1:

$$y = y_0 + \frac{Ae^{\frac{-4\ln(2)(x-x_c)^2}{w^2}}}{w\sqrt{\frac{\pi}{4\ln(2)}}} \qquad [1]$$

where x_c is the center of the EDS peak, A is the amplitude, and w is the full-width at half-maximum. The area under the curve was taken to be a measure of the elemental concentration of the deposit. Due to variability in EDS yield of the different elements, we solely report the carbon content normalized to a standard EBID deposit's carbon content to give an indication of the deposit purity. It is well known that the the Pt-N and C-K EDS peaks overlap. The Pt-N/Pt-M peak ratio was experimentally determined to be approximately 0.03 for our EDS system. This is notably lower than the Pt-N/Pt-M determined by other work to be 0.09, and is likely attributed to a difference in sensitivity of the lower energy portion for the detector. This proportionality constant was used to determine contribution of the Pt-N peak from the Pt-M peak located at 2.048 keV. The estimated contribution of the Pt-N peak was then subtracted from the EDS peak located at 0.277 keV to produce a more accurate estimate of the actual carbon EDS peak.

Results and Discussion

Figure 3 displays the EDS spectra of EBID PtC_5 deposits which were irradiated with the 165 W/cm^2 optical power density, 10 μs pulse width, and 1% duty cycle laser conditions for 0.3 s of laser exposure time. Two conditions are compared where the deposits were laser annealed 1) in the presence of residual chamber gases at a chamber base pressure of 5.2E-6 mbar, in which H_2O is the dominant residual gas, and a 2) localized flow of inert Ar gas. Clearly, the deposit that was annealed under localized Ar ambient experienced greater reduction in carbon content. The localized Ar gas species is inert thus not suspected to contribute to the chemical etching of the carbonaceous matrix within the deposits, however inert gas flow has been shown to increase concentration of residual H_2O adsorbates in the area of localized flux[46]. Hence, the purification mechanism envisioned is a multistep process where (1) Ar gas is locally injected by a GIS, (2) the localized Ar bombards substrate surfaces and enhances the H_2O diffusion rate, (3) H_2O diffuses onto the EBID deposit, and (4) thermal energy supplied by the laser facilitates the dissociation of H_2O into radicals which react with the carbon matrix in PtC_5 deposits and forms volatile compounds which subsequently desorb.

Residual H_2O that contributes toward the thermally driven purification reaction have multiple possible origins from within the system. Specifically H_2O molecules may be supplied from (1) outgassing of chamber walls, (2) outgassing of the substrate, or (3) from contamination in the inert gas line. Figure 3b compares residual gas analysis (RGA) taken of residual chamber gases and during localized Ar flow. Minimal differences in the chamber partial pressure of H_2O (18 amu) molecules with and without localized Ar (20 and 40 amu) flow suggests that the H_2O species which contribute toward the purification process are not delivered from the inert gas line. Inert gas flow localized to the substrate as well as non-localized flow should have similar effect at facilitating H_2O outgassing at the chamber walls. Additional laser anneals of PtC_5 deposits with non-localized Ar flow shows minimal purification (see supporting information), and thus rules out enhanced contribution from H_2O from the chamber wall. Hence, we conclude that the localized Ar gas flux supplied from the GIS needle facilitates the localized enhanced surface diffusion of H_2O from the substrate, which is the dominant contributor toward the purification reaction.

Figure 4 illustrates the integrated normalized carbon EDS peak for various PtC_5 deposit thicknesses as a function of laser exposure (and process) time. The deposits were irradiated with 165 W/cm^2 optical power density, 10 μs pulse width, and 1% duty cycle laser conditions in the localized Ar ambient. The PtC_5 EBID deposits used in this study had a 500 x 500 nm^2 area with variable deposit thickness (~25, 50, 90, and 240 nm by varying the number of EBID passes). As shown previously[48], laser annealing with no localized gas flow does not eliminate the carbon. We also demonstrated, for O_2-laser annealing, that the PtC_5 deposit purification as a function of total laser exposure time (duty cycle x process time) is highly dependent on the initial deposit thickness; thicker deposits anneal faster due to enhanced optical coupling of the laser to the PtC_5 (see supplemental info of Ref [48] for detailed explanation of the role of these material parameters on the laser purification process). A similar behavior is demonstrated here, where the thicker deposits anneal at a faster rate due to enhanced photothermal heating of the deposit.

The purification evolution as a function of depth into EBID deposits were examined in Figure 5. Specifically, 240 nm thick PtC_5 deposits were irradiated with the 10 μs, 1% duty cycle pulsed-laser under flux from Ar inert gas. Deposit cross-sections are shown for 0.2 s and 1.5 s laser exposure times. For these exposure times, the purification front progresses into the deposit, but does not anneal the entire deposit. The proposed purification reactions upon the formation of radicals from H_2O dissociation are as follows:

$$PtC_5(H) + H_2 \overset{hv}{\rightarrow} Pt(s) + CH_4 + hydrocarbons \qquad (1)$$

$$PtC_5(H) + O \quad \overset{hv}{\rightarrow} Pt(s) + H_2O + CO_x + CO_xH_y \qquad (2)$$

for the (1) hydrogenation and (2) oxidation purification reactions, respectively, where $PtC_5(H)$ denotes the hydrogenated PtC_5 deposits. It is worth noting that a self-hydrogenation co-reaction may also play a role during purification due to residual hydrogen present in the amorphous carbon from the original EBID process. Under laser-irradiation and applied heat, dehydrogenation of some ligands result in the hydrogenation and hence volatilization of other ligands producing CH_x or CO_xH_y by-products[53], thus possibly contributing a secondary role in the purification. Dehydrogenation of the amorphous carbon matrix can also result in the formation of additional water molecules under oxygen flux, which may also be tertiary reactions contributing toward the overall purification reaction[31].

Figure 5b is a plot of the purified platinum thickness as a function of laser exposure time for the pulsed laser purifications. To sustain the top-down subsurface purification reaction, the transport of the reactive gas to the reaction front is envisioned to occur via a two-step process, namely: (1)

the reactive gas radicals adsorbs onto the purified Pt surface after thermal dissociation of H_2O molecules and (2) subsequently diffuses to the purification front through the nanoscale porosity that develops. There is also likely purification contribution from H_2O molecules which adsorb and diffuse into the deposit prior to dissociation. Since Pt serves as a catalyst for many hydrogenation and oxidation reactions[54,55], these species will readily chemisorb onto the deposit surface. Therefore, as the Pt surface layer thickens, diffusion of the reactive species to the purification front is expected to be the rate limiting transport mechanism. Recently, purification simulations interrogating the PtC_5/O_2 interaction have revealed that transport is dictated by the cyclic process of dissociation chemisorption/associative desorption on Pt surfaces coupled with O_2 diffusion between Pt interactions[56]. This combined process can be described using an effective diffusion coefficient which is typically much smaller than the diffusion of the gas alone. We suspect that the coupled diffusion process is similar for both reactive gas radicals active here, O and H. The inset plot in Figure 5b plots the purification depth squared as a function of laser exposure time. Since the diffusion depth of the reactive gas species into a material has a $\sqrt{Dt}$ dependence, the linearity ($R^2 = 0.9998$) of the plot is consistent with a diffusion limited purification rate. Hence the diffusion limited purification rate reveals the need for in-situ deposition and purification processes for thick deposits because the time required for diffusion of reactive gas species into the interior of the deposit follows a squared dependency with the depth.

Roberts et al. developed a pulsed-laser assisted process for in-situ purification of EBID deposits, namely Laser Assisted Electron-Beam-Induced Deposition (LAEBID)[47,57]. In this work, laser pulses were synchronized with EBID passes and the highest purity (~37 at% Pt) was achieved when the EBID layer thickness per laser pulse was approximately a monolayer of deposited material. Importantly, the deposits were grown on a titanium film which facilitates the optically coupling and subsequent heating necessary for the thermally driven purification. Nonetheless, even with a monolayer-by-monolayer purification approach, carbon content remained in the deposits (optimum purification realized ~ PtC_2). To try promoting further purification, here we introduce a reactive gas to the LAEBID process. We envision the reactive gas assisted LAEBID process as a direct-write atomic layer deposition (ALD) process with an electron-beam dictated first half-reaction followed by a reactive gas purification second half-reaction dictated by laser heating. Ar inert gas was injected simultaneous with the precursor gas to provide a co-flow (using two individual injection systems) of species necessary for deposition and purification, where once again, the Ar species increases the localized diffusion of H_2O reactive to the deposit. Notably, subsequent studies revealed that precise synchronization and laser pulsing during the refresh time of the EBID layer is not necessary since the electron beam is only irradiating a single pixel while the laser pulse irradiates the entire deposit. This effectively gives refresh time for the other pixels, which have no interaction with the electron beam at that moment in time. Thus the results presented here were not synchronized with the refresh time.

Figure 6a shows a SEM image of a deposit following reactive LAEBID (100 μs pulse width and 0.1% duty cycle). The deposit demonstrates exceptional shape retention and smoothness. In addition, a decrease in carbon content relative to standard PtC_5 EBID resulted (figure 6b). A variety of laser conditions were explored for the reactive LAEBID process in an attempt to promote further purification of the deposits. Changing the duty cycle from 0.1% to 0.5% for 100 μs pulse width (red bars) resulted in a decrease in carbon content from 53 % (relative to standard EBID) to 38 % by providing a greater laser exposure time during deposition. To increase the laser exposure time relative to the EBID half-reaction, an additional 13 ms refresh time after each pass of deposition (yellow bars) was added to further purify the deposits. During the refresh time, the electron beam was blanked and only the laser anneal half-reaction occurs. The added refresh time resulted in a further reduction of carbon. However, the increase in cumulative laser exposure also resulted in laser-assisted chemical vapor deposition (LCVD) in the laser irradiation area (~100μm) as shown in Figure 6b. Therefore, the deposit thickness evolves from a convolution of LAEBID and LCVD processes and results in a loss of deposit shape retention. Additional information on the competing LCVD phenomenon is detailed in the Supplemental Information.

The reactive LAEBID process was also attempted with a pulse width of 10 μs and a variable duty cycle of 1, 3, and 6 % (blue bars). The 10 μs pulse width yields a lower maximum deposit temperature (~490 K) relative to the 100 μs pulse width (~600 K) due to the non-steady state behavior of the laser heating[48]. Higher duty cycles can be tolerated at 10 μs, relative to 100 μs, since less time is required for recovery to room temperature between pulses. Thermal pulse interactions are intentionally avoided in order to both simplify the interpretation of results and avoid a steady state temperature transient over the process time which can favor both LCVD and thermal drift.

Increasing the duty cycle of the 10 μs pulses to 6 % resulted in a reduction in the carbon content of the deposit from 60 % to 25 % relative to standard EBID, which represents the highest purity obtained in our Pt LAEBID deposits that excludes LCVD effects. Beyond 6 % duty cycle resulted in steady state heating and thermal drift during the LAEBID process. Summarily, reactive LAEBID realized a reduction in carbon content of 75 % relative to standard EBID, however complete carbon removal was not achieved. The challenges preventing complete purification are addressed below.

To understand the effect that the $MeCpPtMe_3$ precursor gas had on the photo-thermal half-reaction in the LAEBID process, standard EBID PtC_5 patterns were grown and subsequent laser anneals were carried out with (1) the Ar inert gas flow alone, and (2) a co-flow of Ar reactive gas and $MeCpPtMe_3$ precursor where the precursor nozzle was positioned at approximately 7 mm from the center of field of view and 5 mm above the substrate, sufficient to significantly decrease the $MeCpPtMe_3$ flux as evidenced by a significant decrease in the EBID growth rate at this position. Figure 7 is a plot of the normalized carbon content of the laser annealed deposits as a function of laser exposure time irradiated with 100 μs pulse width and 0.1% duty cycle pulses. Clearly, when annealed with the Ar flow alone, the purification rate is fast relative to the sample laser annealed with the precursor gas co-flow. It is therefore deduced that the presence of the precursor molecule attenuates the purification reaction, thus making complete carbon removal in the reactive gas assisted LAEBID process challenging.

The schematics shown in Figure 8 illustrate a proposed mechanism for the laser-annealing attenuation exhibited when a co-flow of reactive gas/precursor molecules is used. Figure 8a illustrates the common microstructure of PtC_5 deposits, namely platinum nanograins are embedded within an amorphous carbon matrix. In the presence of the Ar gas flux, residual H_2O molecules adsorbed to the substrate exhibit enhanced diffusion rates which reduce the reactive gas replenishment time. Radicals created upon dissociation of H_2O molecules, then react with the carbonaceous matrix through hydrogenation and oxidation reactions to reduce embedded carbon content. When a reactive and precursor gas co-flow is used (Fig. 8c), the relative residence times of the gas molecules on a surface must be considered to realize the resultant equilibrium surface coverage. Large molecules, such as the $MeCpPtMe_3$ precursor used in this study, have longer residence times on the deposit surface than the dissociation H^* and O^* radicals. As the schematic illustrates, the precursor molecules dominate the surface coverage on the deposit surface due to their long residence time (τ). This effectively lowers the coverage of the reactive gas by reducing available adsorption sites and attenuates the purification reaction. Understanding that the co-flow of precursor gas in the presence of reactive gas species attenuates the purification reaction helps explain why the complete LAEBID reaction is limited under laser conditions that would otherwise purify an EBID deposit. This suggests that a pulsed gas procedure is necessary for the in-situ growth and purification of EBID deposits, similar to true atomic layer deposition (ALD) process.

To circumvent the apparent gas competition issues with co-flow, a pulsed gas procedure was utilized in a sequential EBID deposition and subsequent laser anneal process. Specifically, precursor gas was injected during the EBID half-reaction, which was subsequently pumped from the chamber. The precursor partial pressure introduced during this half reaction was ~ 9.0×10^{-6} mbar. A 30 keV beam energy was used for EBID to prevent significant peripheral deposition, which is characteristic of a 5 keV beam with larger beam tails (see Fig. S4). Next, the Ar inert gas was injected at a partial pressure of ~1.2×10^{-5} mbar during the photo-thermally induced de-carburization second half-reaction to enhance diffusion of residual water molecules. Importantly, 10 μs pulse width and 1% duty cycle laser condition were used to anneal the deposit during each cycle, followed by several 100 μs pulse width smoothing pulses. The 10 μs pulses facilitate the de-carburization of the deposit, however, the relatively brief pulses prevent significant coalescence of the Pt, thus promoting deposit shape retention. Several 100 μs pulses are used to promote controlled coalescence after each purification cycle to reduce some deposit porosity whilst maintain shape retention. This cycle was repeated to build a pure deposit of desired size and shape, as illustrated in Figure 1c. Unique to this process compared to a traditional surface reaction limited ALD processes, the number of monolayers deposited per cycle is dictated by EBID half-reaction, which makes sub-monolayer resolution possible. The number of monolayers deposited per cycle largely effects the deposit characteristics as shown in the supporting information (Fig. S4). Due to the ~70% volumetric loss during the decarburization reaction, significant internal stresses will be exhibited in the deposits if many (> 200) monolayers are deposited per cycle. Large internal stresses may cause the deposit to delaminate from the substrate (Fig. S4c), hence there is an optimum number of monolayers per cycle that will result is an acceptable deposition rate whilst preventing significant internal stresses from building up during the purification cycle. Figure 9a displays a pattern deposited using five cycles and ~70 monolayers of deposition per cycle before 100 μs smoothing laser pulses were utilized to reduce porosity of the freshly deposited material from the cycle. Figure 9b displays the deposit after the smoothing pulses were applied. The yellow dotted line denotes the EBID raster pattern. Clearly, precise shape retention is achieved using this sequential deposition technique. Figure 9c is a tilted scanning electron image (52^o) of the deposit, and the total thickness of the purified deposit is estimated to be ~ 50 nm (consistent with the ~ 70% volume reduction experienced when purifying a PtC_5 deposit). EDS spectra of sequential deposition patterns (supplemental information Fig. S4) reveal that the deposits are pure platinum. Hence the sequential deposition process can be utilized to direct write pure nanostructures.

The throughput of the layer by layer process seems noticeably lower than that of a single EBID deposition followed by a subsequent reactive gas anneal, however the completeness of the anneal must be considered. Since the time for diffusion of a reactive gas species to deposit interior is proportional to the depth squared, it may be quite timely to anneal a single standard EBID deposit in its entirety and may result in the lack of shape retention. The throughput of the sequential layer by layer process also has a similar throughput to the completely insitu LAEBID process. This is because the deposition rate may be hindered in the LAEBID process because the elevated substrate temperature reduces gas residence time (for precursor and reactive gas species). To comment briefly, the throughput of the sequential layer by layer process could be improved with a smaller deposition chamber, similarly to an ALD system. This would increase the pumping rates between cycles, enable a higher frequency cyclic process, and ultimately increase applicability of the process.

Conclusions

In conclusion, we have demonstrated a localized pulsed laser-induced purification reaction which can be used to purify PtC_5 EBID deposits generated via electron stimulated reactions of the $MeCpPtMe_3$ precursor. The reactive gas species was supplied by the thermal dissociation of residual H_2O molecules in the chamber, where inert Ar gas was used to enhance H_2O diffusion to the reaction zone.   We have also demonstrated two direct write pseudo atomic layer deposition processes. Specifically, we have presented a reactive gas assisted LAEBID process which is capable of depositing patterns from the $MeCpPtMe_3$ precursor with much greater purity than standard EBID, by utilizing intermittent 915 nm annealing laser pulses and residual H_2O molecules. We have also demonstrated a sequential deposition process to circumvent gas competition for adsorption sites that appears ubiquitous with the LAEBID process. The sequential deposition process utilized a pulsed gas strategy, similar to a traditional ALD process, however for this work, the first half reaction was dictated by electron beam irradiation and the second half reaction was dictated via a photothermally induced purification reaction. The sequential deposition process was successful in deposition of pure nanostructures with high shape retention and fidelity.

As for our perspective on future development of this process, several parameters can surely be further optimized for higher efficiency and throughput. The 915 nm laser is largely transparent to oxide substrates as well as highly reflective on metallic substrates and deposits. Therefore photothermal heating from this laser system is often inefficient. We speculate that lasers in the visible spectrum will heat the substrate or deposits with greater efficiency, thus increasing the throughput of the in-situ and ex-situ annealing strategies of EBID deposits. In the gas co-flow LAEBID process, gas competition for adsorption sites between the reactive gas and precursor gas limits the deposit's purity. This suggests that flux of the reactive gas is not sufficient in comparison to the precursor gas to enable complete deposit purification. A similar setup in an environmental SEM enables the use of pressure regimes (not possible in a standard SEM) which may provide a gas mixture possible of facilitating complete purification in the LAEBID process.

Associated Content

Supporting information

Synchronization maps for laser and electron beam for the laser-assisted electron-beam-induced deposition process, additional details for the LAEBID process, details about contribution of laser-assisted chemical vapor deposition, additional details about the sequential or layer-by-layer EBID process and images. This material is available free of charge via the Internet at http://pubs.acs.org.

Author Information

Corresponding Author

*Email: prack@utk.edu

Acknowledgements

The authors acknowledge that the research was conducted at the Center for Nanophase Materials Sciences, which is a DOE Office of Science User Facility. MGS acknowledges support from the National Defense Science and Engineering Graduate Fellowship funded through the AFOSR. BBL acknowledges support via the University of Tennessee Chancellor’s Fellowship program. PDR and JHN acknowledge support from Intel Corporation (and Shida Tan as program mentor).

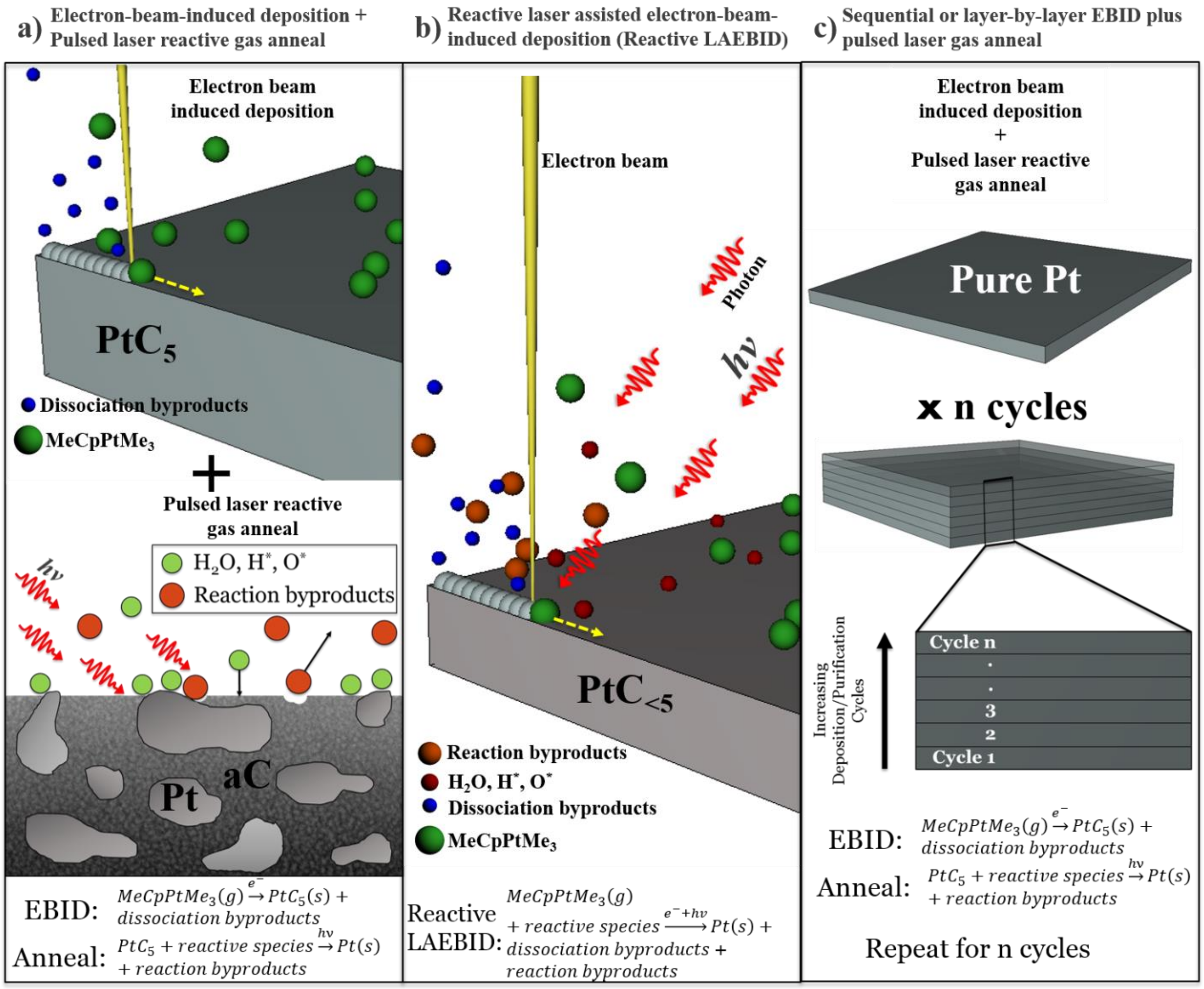

Figure 1. Schematic of the (a) EBID + pulsed laser reactive gas anneal, (b) reactive laser assisted electron-beam-induced deposition, and (c) sequential or layer-by-layer EBID plus laser reactive gas anneal purification processes.

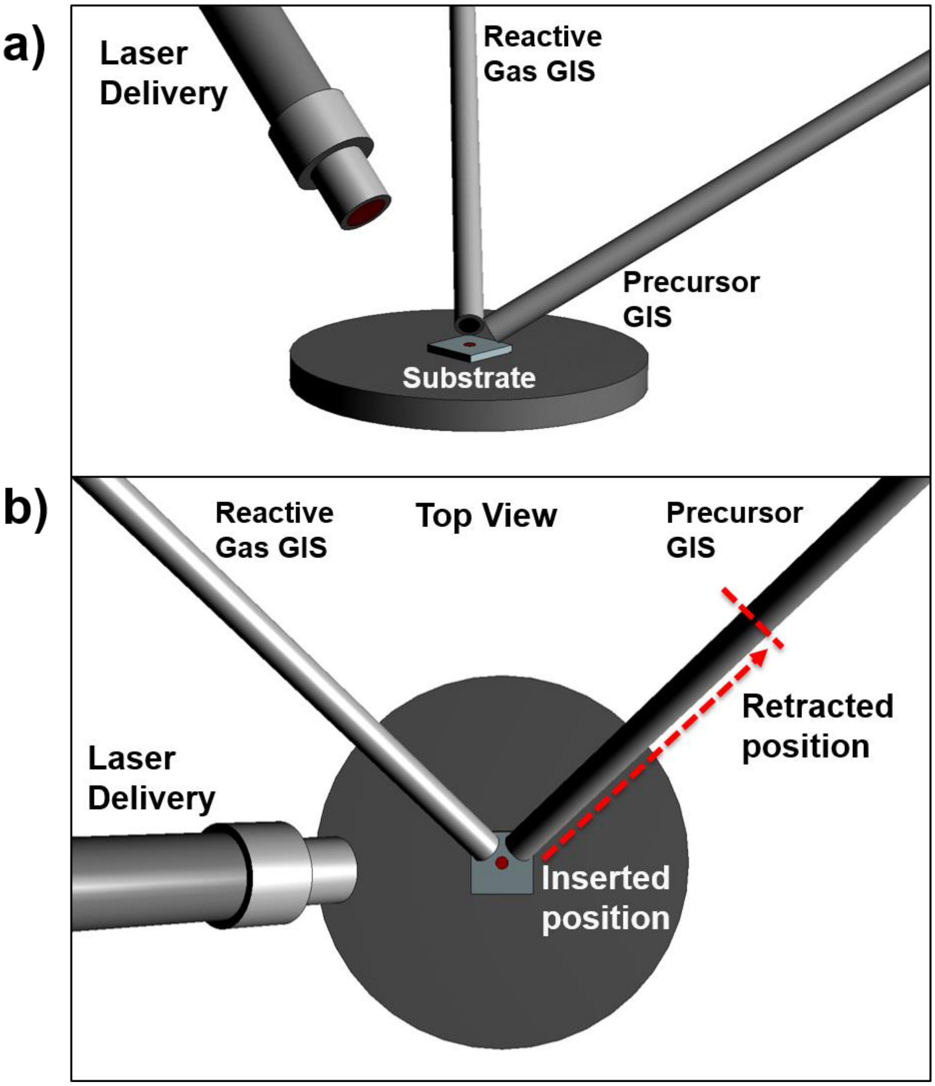

Figure 2. Schematic of deposition and annealing experimental setup from (a) tilted and (b) plan view. The laser delivery system, focused electron beam, precursor GIS, and reactive gas GIS converge to a single point. During reactive LAEBID processes the precursor GIS needle is in the "retracted" position (dotted red line) which is withdrawn to ~8 cm vertically and ~5 cm horizontally from the point of interest to reduce precursor flux at the substrate. During the sequential deposition plus annealing process the needles are configured in the as-shown inserted states.

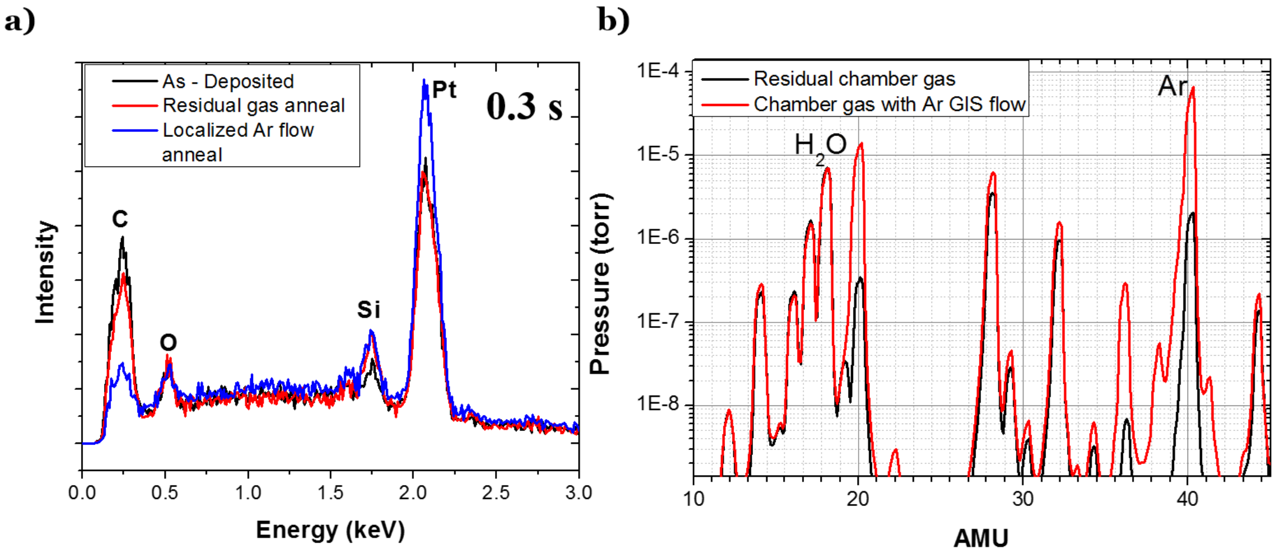

Figure 3. (a) EDS spectra of Pt EBID deposits which were annealed with 10 us and 1% duty cycle laser conditions for a cumulative laser exposure time of 0.3 s. Spectra shown include an as-deposited pattern, a deposit anneal under chamber ambiance, and a deposit annealed under localized Ar gas flow. (b) RGA spectra showing the residual chamber gas species present as well as during Ar flow.

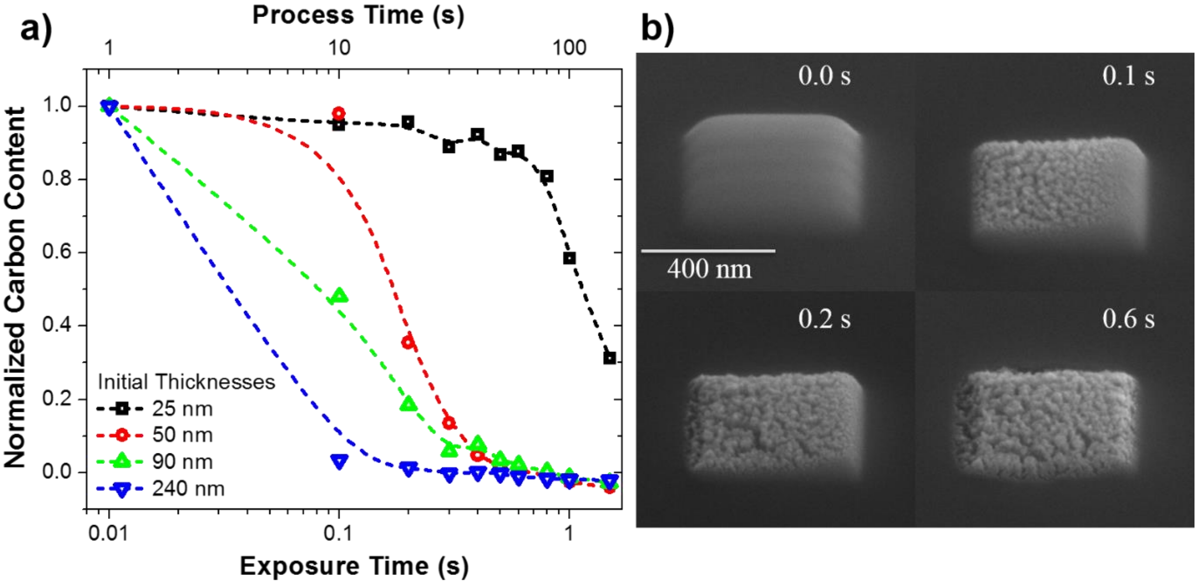

Figure 4. (a) Carbon content, from EDS measurements, as a function of laser exposure time (duty cycle x processing time, bottom axis) and processing time (top axis) for 10 μs at 1% laser duty cycle. The deposit thicknesses were approximately 240 nm, 90 nm, 50 nm, 25 nm which correspond to 8000, 4000, 2000, and 1000 passes, respectively. Normalized carbon content of 1, is that of a standard PtC_5 EBID deposit. (b) SEM images of an annealed deposit that was initially ~ 90 nm as-deposited. Inset time reflects the total laser exposure time for each anneal.

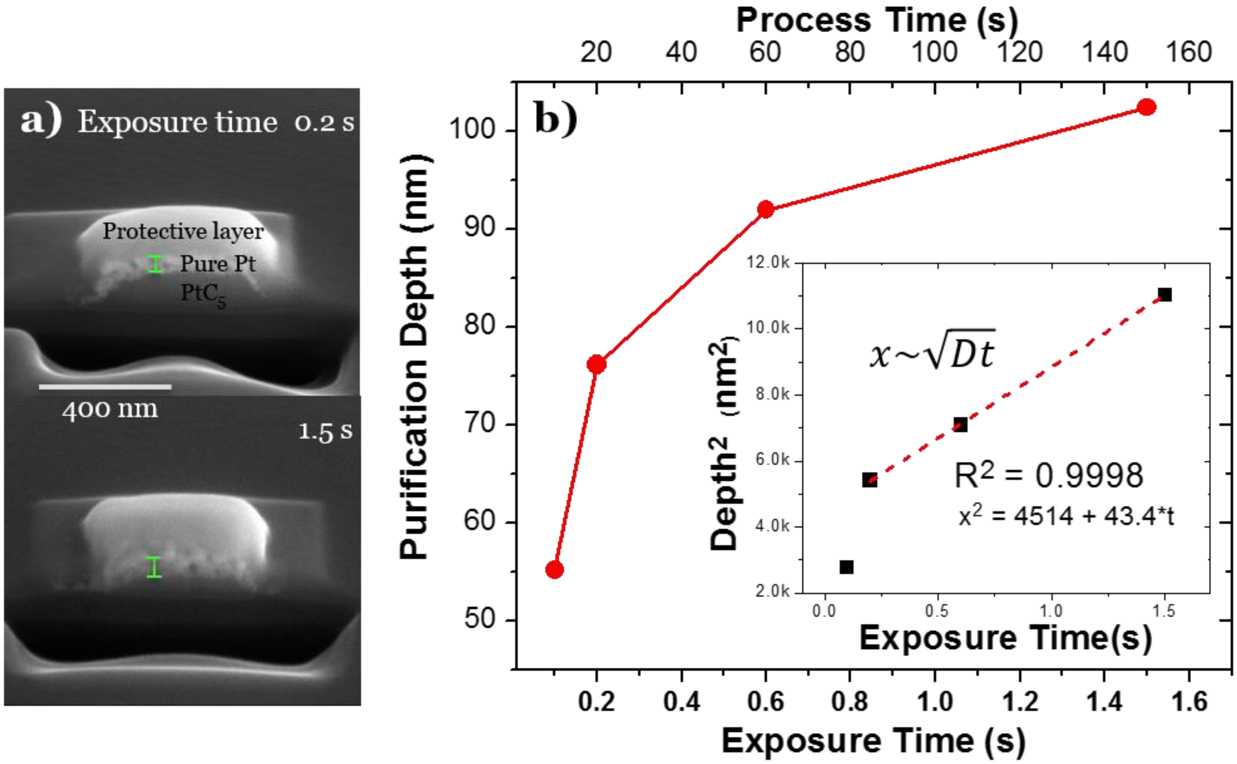

Figure 5. (a) SEM cross section images of deposits annealed with reactive gas for 0.2 s and 1.5 s of total laser exposure time. (b) Purification thickness from an originally ~ 240 nm thick PtC_5 deposit as a function of pulsed laser exposure time for a 10 µs, 1% duty cycle anneal while under Ar gas flow. Inset figure shows the plot and linear regression of purification thickness squared versus time which is consistent with a diffusion limited purification regime.

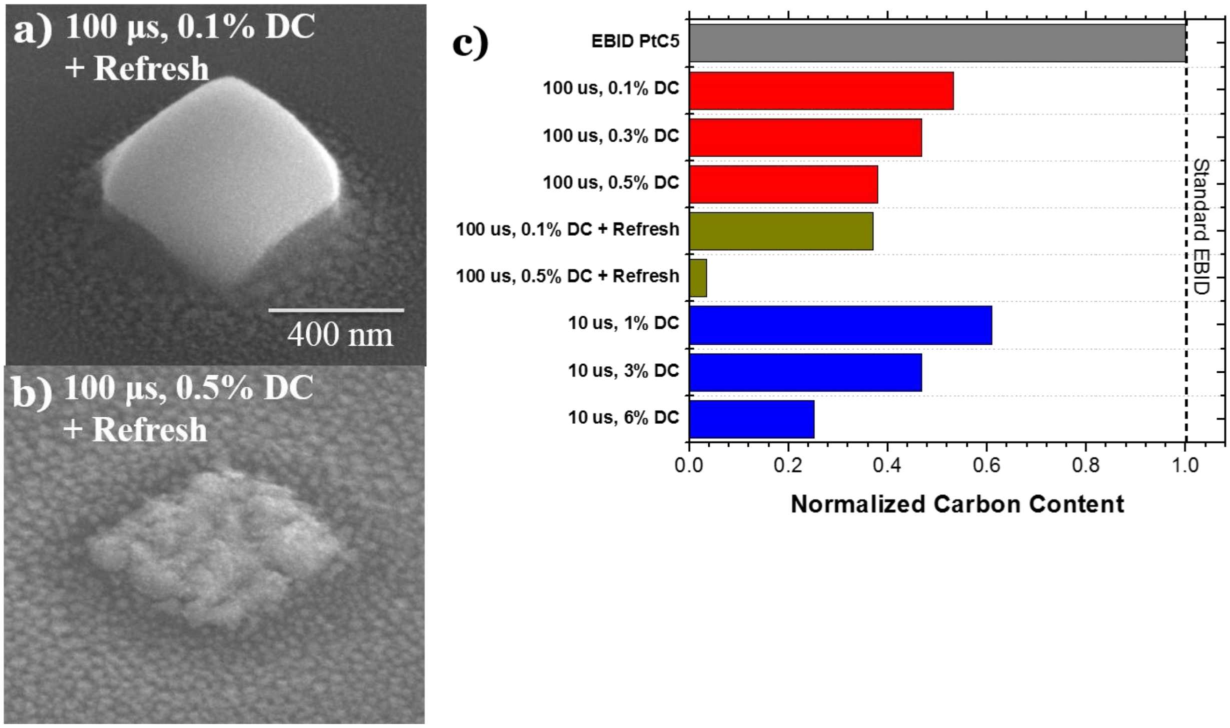

Figure 6. (a) SEM tilt image of a typical laser assisted electron beam induced deposition (LAEBID) pattern deposited with co-flow of hydrogen reactive gas. Specifically, this deposit was created 100 µs and 0.1% duty cycle laser conditions. The electron beam and gas conditions were as listed in the experimental details. (b) SEM image of a LAEBID pattern deposited with 100 µs and 0.5% duty cycle laser conditions, which shows contribution from LCVD. The deposit retains shape with high fidelity. (c) Comparison of LAEBID patterns deposited with various laser and refresh parameters. Refresh denotes extra time between LAEBID passes to enhance the laser-on time relative to the EBID time. Additional process parameter information may be found in the supporting information.

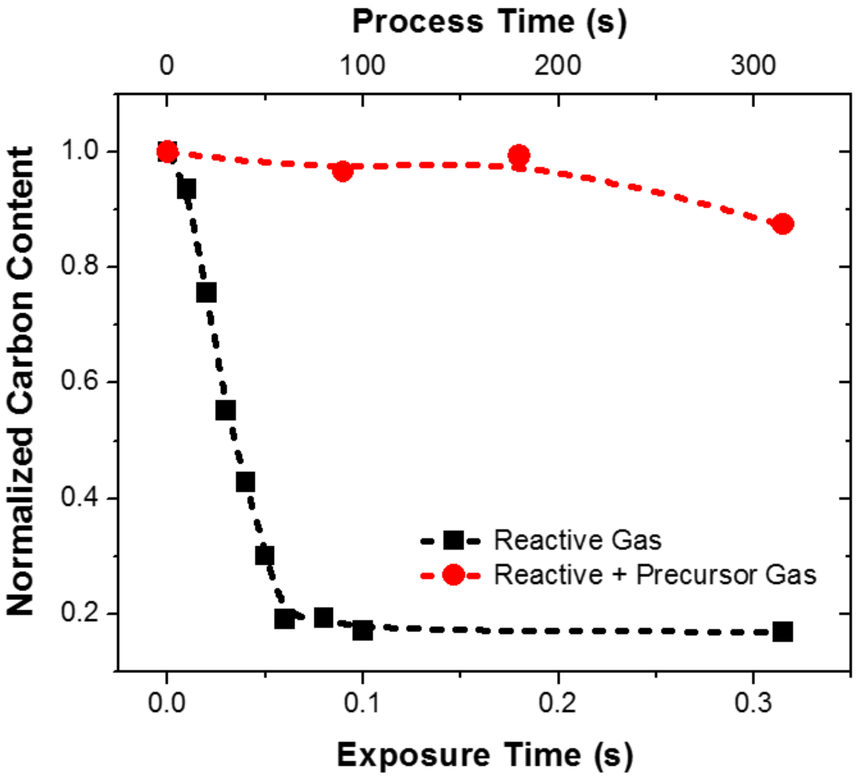

Figure 7. Normalized carbon content for standard EBID deposits annealed in reactive gas only (black) and a co-flow with approximately equal localized pressure of reactive gas plus the organometallic $MeCpPtMe_3$ precursor (red). Deposits were annealed with 100 µs, 0.1% laser duty cycle conditions.

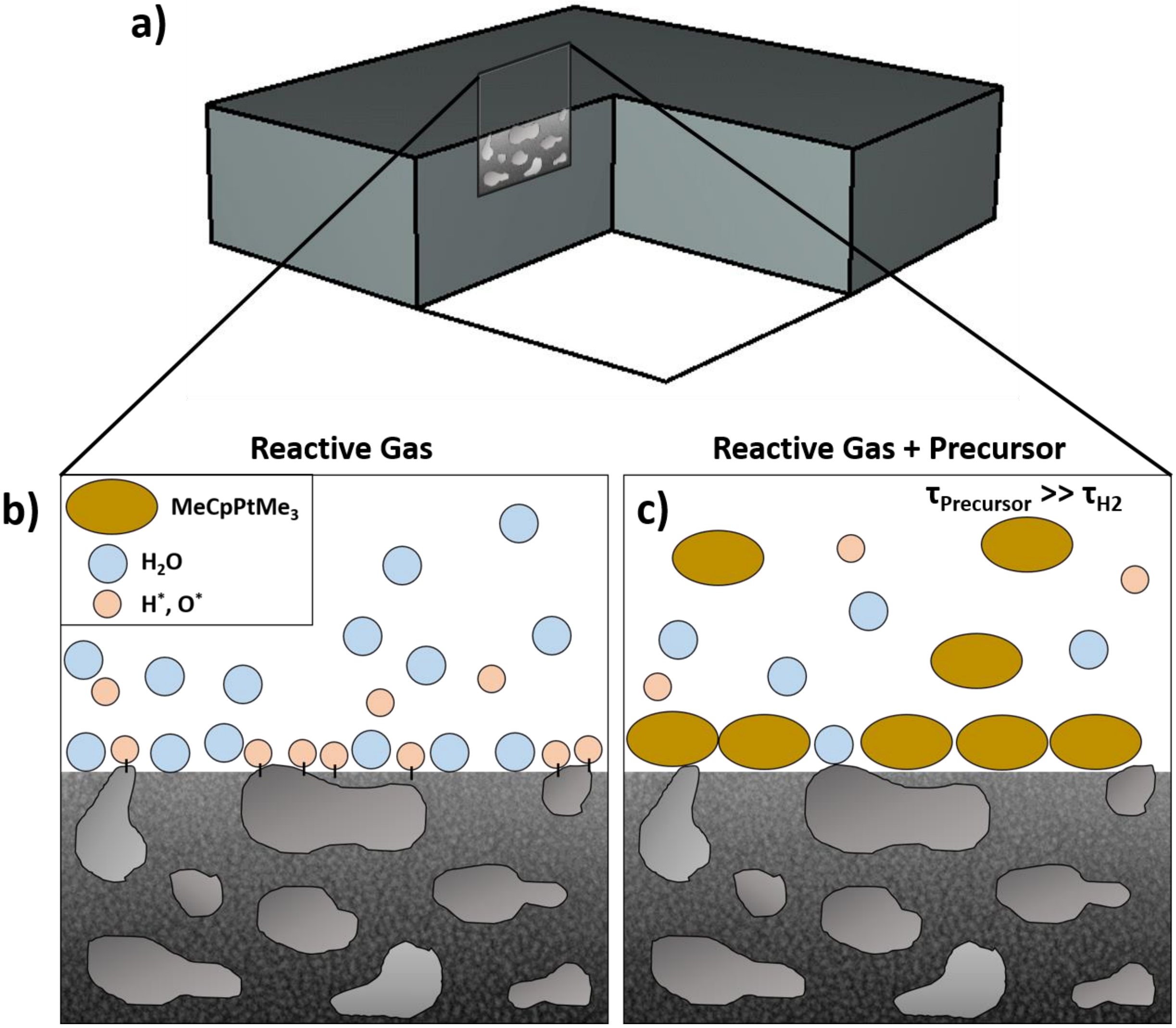

Figure 8. Schematic of proposed purification retardation mechanism. (a) EBID PtC_5 deposit is composed of Pt nanoparticles suspended with in an amorphous carbon matrix. (b) Under a flux of molecular H_2O only, there are many adsorption sites for the purification reaction to occur. (c) With a co-flow of H_2O and $MeCpPtMe_3$, the $MeCpPtMe_3$precursor gas dominates the surface coverage due to the long residence time and occupies many adsorption sites and reduces purification rate.

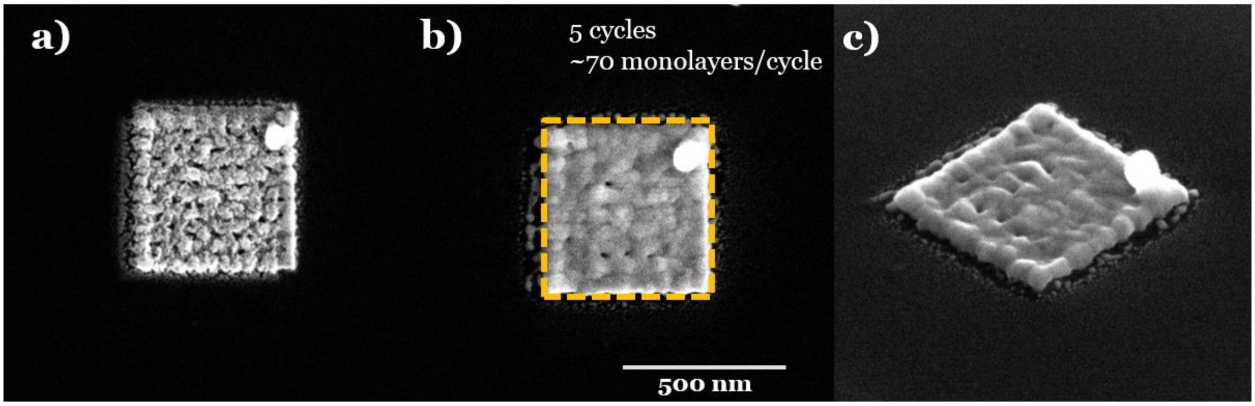

Figure 9. Sequential deposit fabricated from 5 cycles with approximately 70 monolayers deposited per cycle (a) before and (b) after 100 μs smoothing pulses were applied to reduce porosity of the deposit. Inset dashed square denotes original pattern shape prescribed by EBID raster sequence. (c) SEM tilted image (52^o) of the sequential deposit.

(1) Botman, A.; Mulders, J. J. L.; Hagen, C. W. Creating Pure Nanostructures from Electron-Beam-Induced Deposition Using Purification Techniques: A Technology Perspective. *Nanotechnology* **2009**, *20*.

(2) Utke, I.; Moshkalev, S.; Russell, P. *Nanofabrication Using Focused Ion and Electron Beams: Principles and Applications*; Oxford University Press, 2012.

(3) Randolph, S. J.; Fowlkes, J. D.; Rack, P. D. Focused, Nanoscale Electron-Beam-Induced Deposition and Etching. *Crit. Rev. Solid State Mater. Sci.* **2006**, *31*, 55–89.

(4) Toth, M.; Lobo, C. J.; Hartigan, G.; Knowles, W. R. Electron Flux Controlled Switching between Electron Beam Induced Etching and Deposition. *J. Appl. Phys.* **2007**, *101*, 54309.

(5) Fowlkes, J. D.; Rack, P. D. Fundamental Electron-Precursor-Solid Interactions Derived from Time-Dependent Electron-Beam-Induced Deposition Simulations and Experiments. *ACS Nano* **2010**, *4*, 1619–1629.

(6) Utke, I.; Friedli, V.; Purrucker, M.; Michler, J. Resolution in Focused Electron- and Ion-Beam Induced Processing. *J. Vac. Sci. Technol. B* **2007**, *25*, 2219–2223.

(7) Smith, D. A.; Fowlkes, J. D.; Rack, P. D. Understanding the Kinetics and Nanoscale Morphology of Electron-Beam-Induced Deposition via a Three-Dimensional Monte Carlo Simulation: The Effects of the Precursor Molecule and the Deposited Material. *Small* **2008**, *4*, 1382–1389.

(8) Hoeflich, K.; Yang, R. Bin; Berger, A.; Leuchs, G.; Christiansen, S. The Direct Writing of Plasmonic Gold Nanostructures by Electron-Beam-Induced Deposition. *Adv. Mater.* **2011**, *23*, 2657+.

(9) Choo, H.; Kim, M. K.; Staffaroni, M.; Seok, T. J.; Bokor, J.; Cabrini, S.; Schuck, P. J.; Wu, M. C.; Yablonovitch, E. Nanofocusing in a Metal-Insulator-Metal Gap Plasmon Waveguide with a Three-Dimensional Linear Taper. *Nat. Photonics* **2012**, *6*, 837–843.

(10) Koops, H. W. P.; Schossler, C.; Kaya, A.; Weber, M. Conductive Dots, Wires, and Supertips for Field Electron Emitters Produced by Electron-Beam Induced Deposition on Samples Having Increased Temperature. *J. Vac. Sci. Technol. B* **1996**, *14*, 4105–4109.

(11) Yang, X.; Simpson, M. L.; Randolph, S. J.; Rack, P. D.; Baylor, L. R.; Cui, H.; Gardner, W. L. Integrated Tungsten Nanofiber Field Emission Cathodes Selectively Grown by Nanoscale Electron Beam-Induced Deposition. *Appl. Phys. Lett.* **2005**, *86*, 183106.

(12) Guan, Y.; Fowlkes, J. D.; Retterer, S. T.; Simpson, M. L.; Rack, P. D. Nanoscale Lithography via Electron Beam Induced Deposition. *Nanotechnology* **2008**, *19*.

(13) Mackus, A. J. M.; Thissen, N. F. W.; Mulders, J. J. L.; Trompenaars, P. H. F.; Verheijen, M. A.; Bol, A. A.; Kessels, W. M. M. Direct-Write Atomic Layer Deposition of High-Quality Pt Nanostructures: Selective Growth Conditions and Seed Layer Requirements. *J. Phys. Chem. C* **2013**, *117*, 10788–10798.

(14) Rykaczewski, K.; Hildreth, O. J.; Kulkarni, D.; Henry, M. R.; Kim, S. K.; Wong, C. P.; Tsukruk, V. V; Fedorov, A. G. Mask Less and Resist-Free Rapid Prototyping of Three-Dimensional Structures Through Electron Beam Induced Deposition (EBID) of Carbon in Combination with Metal-Assisted Chemical Etching (MaCE) of Silicon. *ACS Appl. Mater. Interfaces* **2010**, *2*, 969–973.

(15) Seki, Y.; Furuta, Y.; Nishikawa, H.; Watanabe, T.; Nakata, T.; Satoh, T.; Ishii, Y.; Kamiya, T. Electroplating Using High-Aspect-Ratio Microstructures Fabricated by Proton Beam Writing. *Microelectron. Eng.* **2009**, *86*, 945–948.

(16) Lassiter, M. G.; Liang, T.; Rack, P. D. Inhibiting Spontaneous Etching of Nanoscale Electron Beam Induced Etching Features: Solutions for Nanoscale Repair of Extreme Ultraviolet Lithography Masks. *J. Vac. Sci. Technol. B* **2008**, *26*, 963–967.

(17) Liang, T.; Frendberg, E.; Lieberman, B.; Stivers, A. Advanced Photolithographic Mask Repair Using Electron Beams. *J. Vac. Sci. Technol. B* **2005**, *23*, 3101–3105.

(18) Noh, J. H.; Stanford, M. G.; Lewis, B. B.; Fowlkes, J. D.; Plank, H.; Rack, P. D. Nanoscale Electron Beam-Induced Deposition and Purification of Ruthenium for Extreme Ultraviolet Lithography Mask Repair. *Appl. Phys. A* **2014**, *117*, 1705–1713.

(19) Bret, T.; Afra, B.; Becker, R.; Hofmann, T.; Edinger, K.; Liang, T.; Hoffmann, P. Gas Assisted Focused Electron Beam Induced Etching of Alumina. *J. Vac. Sci. Technol. B* **2009**, *27*, 2727–2731.

(20) Utke, I.; Hoffmann, P.; Berger, R.; Scandella, L. High-Resolution Magnetic Co Supertips Grown by a Focused Electron Beam. *Appl. Phys. Lett.* **2002**, *80*, 4792–4794.

(21) Noh, J. H.; Nikiforov, M.; Kalinin, S. V; Vertegel, A. A.; Rack, P. D. Nanofabrication of Insulated Scanning Probes for Electromechanical Imaging in Liquid Solutions. *Nanotechnology* **2010**, *21*.

(22) Makise, K.; Mitsuishi, K.; Shimojo, M.; Shinozaki, B. Microstructural Analysis and Transport Properties of MoO and MoC Nanostructures Prepared by Focused Electron Beam-Induced Deposition. *Sci. Rep.* **2014**, *4*.

(23) Winhold, M.; Weirich, P. M.; Schwalb, C. H.; Huth, M. Superconductivity and Metallic Behavior in PbxCyOδ Structures Prepared by Focused Electron Beam Induced Deposition. *Appl. Phys. Lett.* **2014**, *105*, 162603.

(24) Brintlinger, T.; Fuhrer, M. S.; Melngailis, J.; Utke, I.; Bret, T.; Perentes, A.; Hoffmann, P.; Abourida, M.; Doppelt, P. Electrodes for Carbon Nanotube Devices by Focused Electron Beam Induced Deposition of Gold. *J. Vac. Sci. Technol. B* **2005**, *23*, 3174–3177.

(25) Serrano-Ramon, L.; Cordoba, R.; Alfredo Rodriguez, L.; Magen, C.; Snoeck, E.; Gatel, C.; Serrano, I.; Ricardo Ibarra, M.; Maria De Teresa, J. Ultrasmall Functional Ferromagnetic Nanostructures Grown by Focused Electron-Beam-Induced Deposition. *ACS Nano* **2011**, *5*, 7781–7787.

(26) Gavagnin, M.; Wanzenboeck, H. D.; Belic, D.; Bertagnolli, E. Synthesis of Individually Tuned Nanomagnets for Nanomagnet Logic by Direct Write Focused Electron Beam Induced Deposition. *ACS Nano* **2013**, *7*, 777–784.

(27) Wnuk, J. D.; Rosenberg, S. G.; Gorham, J. M.; van Dorp, W. F.; Hagen, C. W.; Fairbrother, D. H. Electron Beam Deposition for Nanofabrication: Insights from Surface Science. *Surf. Sci.* **2011**, *605*, 257–266.

(28) Botman, A.; Hesselberth, M.; Mulders, J. J. L. Improving the Conductivity of Platinum-Containing Nano-Structures Created by Electron-Beam-Induced Deposition. *Microelectron. Eng.* **2008**, *85*, 1139–1142.

(29) Plank, H.; Gspan, C.; Dienstleder, M.; Kothleitner, G.; Hofer, F. The Influence of Beam Defocus on Volume Growth Rates for Electron Beam Induced Platinum Deposition. *Nanotechnology* **2008**, *19*.

(30) Plank, H.; Noh, J. H.; Fowlkes, J. D.; Lester, K.; Lewis, B. B.; Rack, P. D. Electron-Beam-Assisted Oxygen Purification at Low Temperatures for Electron-Beam-Induced Pt Deposits: Towards Pure and High-Fidelity Nanostructures. *ACS Appl. Mater. Interfaces* **2014**, *6*, 1018–1024.

(31) Geier, B.; Gspan, C.; Winkler, R.; Schmied, R.; Fowlkes, J. D.; Fitzek, H.; Rauch, S.; Rattenberger, J.; Rack, P. D.; Plank, H. Rapid and Highly Compact Purification for Focused Electron Beam Induced Deposits: A Low Temperature Approach Using Electron Stimulated H2O Reactions. *J. Phys. Chem. C* **2014**, *118*, 14009–14016.

(32) Takeguchi, M.; Shimojo, M.; Furuya, K. Post-Deposition Processes for Nanostructures Formed by Electron Beam Induced Deposition with Pt(PF3)(4) Precursor. *Appl. Phys. A Mater. Sci. Process.* **2008**, *93*, 439–442.

(33) Porrati, F.; Sachser, R.; Schwalb, C. H.; Frangakis, A. S.; Huth, M. Tuning the Electrical Conductivity of Pt-Containing Granular Metals by Postgrowth Electron Irradiation. *J. Appl. Phys.* **2011**, *109*, 063715.

(34) Belić, D.; Shawrav, M. M.; Gavagnin, M.; Stöger-Pollach, M.; Wanzenboeck, H. D.; Bertagnolli, E. Direct-Write Deposition and Focused-Electron-Beam-Induced Purification of Gold Nanostructures. *ACS Appl. Mater. Interfaces* **2015**, *7*, 2467–2479.

(35) Villamor, E.; Casanova, F.; Trompenaars, P. H. F.; Mulders, J. J. L. Embedded Purification for Electron Beam Induced Pt Deposition Using MeCpPtMe 3. *Nanotechnology* **2015**, *26*, 95303.

(36) Stark, T. J.; Mayer, T. M.; Griffis, D. P.; Russell, P. E. Formation of Complex Features Using Electron-beam Direct-write Decomposition of Palladium Acetate. *J. Vac. Sci. Technol. B* **1992**, *10*, 2685–2689.

(37) Klein, K. L.; Randolph, S. J.; Fowlkes, J. D.; Allard, L. F.; Meyer III, H. M.; Simpson, M. L.; Rack, P. D. Single-Crystal Nanowires Grown via Electron-Beam-Induced Deposition. *Nanotechnology* **2008**, *19*, 345705.

(38) Fernandez-Pacheco, A.; De Teresa, J. M.; Cordoba, R.; Ibarra, M. R. Magnetotransport Properties of High-Quality Cobalt Nanowires Grown by Focused-Electron-Beam-Induced Deposition. *J. Phys. D Appl. Phys.* **2009**, *42*, 055005.

(39) Gopal, V.; Radmilovic, V. R.; Daraio, C.; Jin, S.; Yang, P. D.; Stach, E. A. Rapid Prototyping of Site-Specific Nanocontacts by Electron and Ion Beam Assisted Direct-Write Nanolithography. *Nano Lett.* **2004**, *4*, 2059–2063.

(40) Botman, A.; Mulders, J. J. L.; Weemaes, R.; Mentink, S. Purification of Platinum and Gold Structures after Electron-Beam-Induced Deposition. *Nanotechnology* **2006**, *17*, 3779–3785.

(41) Langford, R. M.; Wang, T. X.; Ozkaya, D. Reducing the Resistivity of Electron and Ion Beam Assisted Deposited Pt. *Microelectron. Eng.* **2007**, *84*, 784–788.

(42) Tseng, A. A. *Nanofabrication: Fundamentals and Applications*; World Scientific, 2008.

(43) Langford, R. M.; Ozkaya, D.; Sheridan, J.; Chater, R. Effects of Water Vapour on Electron and Ion Beam Deposited Platinum. *Microsc. Microanal.* **2004**, *10*, 1122–1123.

(44) Perentes, A.; Hoffmann, P. Focused Electron Beam Induced Deposition of Si-Based Materials from SiOxCy to Stoichiometric SiO2: Chemical Compositions, Chemical-Etch Rates, and Deep Ultraviolet Optical Transmissions. *Chem. Vap. Depos.* **2007**, *13*, 176–184.

(45) Mehendale, S.; Mulders, J. J. L.; Trompenaars, P. H. F. A New Sequential EBID Process for the Creation of Pure Pt Structures from MeCpPtMe3. *Nanotechnology* **2013**, *24*, 145303.

(46) Martin, A.; McCredie, G.; Toth, M. Electron Beam Induced Etching of Carbon. *Appl. Phys. Lett.* **2015**, (in revision).

(47) Roberts, N. A.; Fowlkes, J. D.; Magel, G. A.; Rack, P. D. Enhanced Material Purity and Resolution via Synchronized Laser Assisted Electron Beam Induced Deposition of Platinum. *Nanoscale* **2013**, *5*, 408–415.

(48) Stanford, M. G.; Lewis, B. B.; Noh, J. H.; Fowlkes, J. D.; Roberts, N. A.; Plank, H.; Rack, P. D. Purification of Nanoscale Electron-Beam-Induced Platinum Deposits via a Pulsed Laser-Induced Oxidation Reaction. *ACS Appl. Mater. Interfaces* **2014**, *6*, 21256–21263.

(49) Kanarik, K. J.; Lill, T.; Hudson, E. A.; Sriraman, S.; Tan, S.; Marks, J.; Vahedi, V.; Gottscho, R. A. Overview of Atomic Layer Etching in the Semiconductor Industry. *J. Vac. Sci. Technol. A* **2015**, *33*, 020802.

(50) Roberts, N. A.; Magel, G. A.; Hartfield, C. D.; Moore, T. M.; Fowlkes, J. D.; Rack, P. D. In Situ Laser Processing in a Scanning Electron Microscope. *J. Vac. Sci. Technol. A* **2012**, *30*, 041404.

(51) Plank, H.; Smith, D. A.; Haber, T.; Rack, P. D.; Hofer, F. Fundamental Proximity Effects in Focused Electron Beam Induced Deposition. *ACS Nano* **2012**, *6*, 286–294.

(52) Arnold, G.; Timilsina, R.; Fowlkes, J.; Orthacker, A.; Kothleitner, G.; Rack, P. D.; Plank, H. Fundamental Resolution Limits during Electron-Induced Direct-Write Synthesis. *ACS Appl. Mater. Interfaces* **2014**, *6*, 7380–7387.

(53) Mackus, A. J. M.; Leick, N.; Baker, L.; Kessels, W. M. M. Catalytic Combustion and Dehydrogenation Reactions during Atomic Layer Deposition of Platinum. *Chem. Mater.* **2012**, *24*, 1752–1761.

(54) Xue, Z. L.; Thridandam, H.; Kaesz, H. D.; Hicks, R. F. Organometallic Chemical Vapor Deposition of Platinum. Reaction Kinetics and Vapor Pressures of Precursors. *Chem. Mater.* **1992**, *4*, 162–166.

(55) Sachser, R.; Reith, H.; Huzel, D.; Winhold, M.; Huth, M. Catalytic Purification of Directly Written Nanostructured Pt Microelectrodes. *ACS Appl. Mater. Interfaces* **2014**, *6*, 15868–15874.

(56) Fowlkes, J. D.; Geier, B.; Lewis, B. B.; Rack, P. D.; Stanford, M. G.; Winkler, R.; Plank, H. Electron Nanoprobe Induced Oxidation: A Simulation of Direct-Write Purification. *Phys. Chem. Chem. Phys.* **2015**, DOI: 10.1039/C5CP01196E.

(57) Roberts, N. A.; Gonzalez, C. M.; Fowlkes, J. D.; Rack, P. D. Enhanced by-Product Desorption via Laser Assisted Electron Beam Induced Deposition of W (CO)(6) with Improved Conductivity and Resolution. *Nanotechnology* **2013**, *24*, 415301.

Table of Contents Artwork